Optimizing Sawtooth Electrodes for Ultra-High-Speed Electro-Optic Modulators

Shurui Huang, Deyang Kong, Huijie Sun, Yongzhuo Li, *Member, IEEE*, Xue Feng, Wei Zhang, and Yidong Huang

***Abstract*—Electro-optic (EO) modulators with ultra-high speed and low driving voltage are essential for high-performance optical computing, optical communication, and broadband microwave photonic links. In this work, we have proposed an electrode optimization method for periodic structures, based on the RGLC transmission line model and exemplified by sawtooth traveling-wave electrodes (STWEs). We have established analytical expressions for characteristic parameters including the resistance, inductance, capacitance, as well as the slot depth and width of STWEs for the first time, achieving synchronous optimization of microwave loss minimization and velocity matching. Validated through simulations on thin-film lithium niobate modulators, the approach achieves an ultra-high EO bandwidth of up to 290 GHz and a low voltage-length product of 2.5 V·cm. The optimized STWEs feature a minimum linewidth of 5 μm and a metal thickness as thin as 500 nm, which are compatible with deep ultraviolet lithography and suitable for large-scale, low-cost fabrication. This work would pave the way for developing scalable ultra-high-speed EO modulator arrays.**

***Index Terms*—Electro-optic modulators, integrated photonics, lithium niobate, traveling-wave electrodes.**

I. Introduction

ELECTRO-OPTIC (EO) modulators are fundamental components in modern optical communication and signal processing systems, playing a critical role in high-performance computing, optical phased arrays, and broadband microwave photonic links. With the increasing symbol rates in digital communications and carrier frequencies in analog systems, there is a growing demand for EO modulators that simultaneously offer ultra-high-speed operation and CMOS-compatible low drive voltages.

Over the past few decades, EO modulators based on III–V compound semiconductors [1], [2] and silicon [3], [4] have been extensively investigated. Though these platforms offer relatively high modulation efficiency, they typically suffer from considerable optical insertion loss and microwave absorption. In contrast, lithium niobate (LN) has emerged as a promising material for high-performance EO modulation, thanks to its large EO coefficient (30.8 pm/V), low optical loss, excellent thermal stability, and wide transparency window (350 nm–5 μm) [5]. However, conventional bulk LN modulators rely on weakly confined waveguides with low index contrast (∼0.02), resulting in bulky devices that are not suitable for large-scale integration [6]. The development of thin-film lithium niobate (TFLN) has substantially improved the field confinement and compactness of EO modulators, owing to the high index contrast (>0.7) between the LN core and the cladding layers [7], [8]. Since 2018 [9], TFLN modulators have witnessed rapid advancements, enabling sub-3 V half-wave voltage (V_π) and over 100 GHz EO bandwidth on low permittivity substrates such as quartz, which allow for larger electrode gaps and more uniform current distribution, thereby reducing radio-frequency (RF) losses readily [10], [11]. Compared with quartz and other traditional low permittivity substrates, TFLN modulators on silicon substrates offer significant advantages, including excellent thermal conductivity, mechanical strength, and high compatibility with CMOS fabrication processes [12].

Nonetheless, the performance of current TFLN modulators on silicon substrates remains limited, typically exhibiting bandwidth-to-voltage ratios below 35 GHz/V [13], [14], far below those demonstrated on quartz [10], which severely hinders scaling on silicon-on-insulator (SOI) platforms. In traditional coplanar waveguide (CPW) electrode designs, there is a trade-off between the V_π and bandwidth. For example, a narrower electrode gap can enhance modulation efficiency but also increase microwave loss. For traditional straight-strip CPW electrodes, the degrees of freedom are limited, hindering further performance optimization. To address these limitations, capacitively-loaded traveling-wave electrodes (CL-TWEs) have been proposed and have become one of the most widely adopted designs [15], [16]. Recent demonstrations have shown that a 7 mm TFLN modulator achieves a 3-dB EO bandwidth exceeding 110 GHz and a voltage-length product ($V_\pi L_t$) of 1.33 V·cm, while simulations predict a 6.4-dB electrical bandwidth up to 218 GHz [17]. While CL-TWEs enable high-speed operation with low V_π, their fine T-rail features with minimum linewidths of approximately 1 μm require costly electron beam lithography (EBL) [18]. Additionally, CL-TWEs tend to increase the microwave refractive index significantly, necessitating further design interventions such as introducing low-k dielectric layers (e.g., BCB) [19],

Received 1 August 2025; revised 28 September 2025; accepted 4 October 2025. Date of publication 10 October 2025; date of current version 21 October 2025. This work was supported in part of the National Key Research and Development Program of China under Grant 2023YFB2806703 and in part by the National Natural Science Foundation of China under Grant U22A6004, Grant 92365210, and Grant 62175124. *(Corresponding authors: Yongzhuo Li, Xue Feng, Yidong Huang.)*

The authors are with the Nano-OptoElectronics Lab, Department of Electronic Engineering, Tsinghua University, Beijing 100084, China (e-mail: huangsr24@mails.tsinghua.edu.cn; kdy20@mails.tsinghua.edu.cn; shj23@mails.tsinghua.edu.cn; liyongzhuo@tsinghua.edu.cn; x-feng@tsinghua.edu.cn; zwei@tsinghua.edu.cn; yidonghuang@tsinghua.edu.cn).

Digital Object Identifier 10.1109/JPHOT.2025.3620360

thickening silicon dioxide (SiO_2) buffer layers [20], or even undercutting the silicon substrate to restore velocity matching between the optical and microwave signals [21], [22]. These solutions would increase fabrication complexity and hinder large-scale manufacturability. In contrast, sawtooth traveling-wave electrodes (STWEs) offer several compelling advantages, including greater design flexibility, wider minimum feature sizes ($\sim$4 μm), and compatibility with standard optical lithography, thereby enabling cost-effective wafer-scale fabrication. Previous studies have leveraged the slow-wave effect induced by inductive loading in STWEs to demonstrate a 5 mm hybrid silicon–lithium niobate EO modulator that achieved beyond 110 GHz 3-dB EO bandwidth and a $V_\pi L_t$ of 3.1 V·cm [23]. However, whether employing CL-TWEs or STWEs, previous studies have primarily focused on demonstrating device-level performance, without providing detailed analysis or optimization of the fine structural geometry of the electrodes. To address this gap, we conduct a systematic analysis of STWEs based on the RGLC model, which represents the equivalent transmission line circuit incorporating resistance (R), conductance (G), inductance (L), and capacitance (C). Although the structure of STWEs is not novel, we have provided the analytical expressions linking the RGLC model parameters with the key structural parameters of STWEs for the first time, and establish a theoretical framework to explain how key geometrical features of the STWEs influence the corresponding electromagnetic behavior.

In this work, we break the voltage-bandwidth trade-off limit in TFLN modulators on silicon substrates with optimized STWEs that simultaneously minimize microwave loss and achieve optimal velocity matching. Our design achieves a simulated 3-dB EO bandwidth of approximately 290 GHz, while maintaining a low $V_\pi L_t$ of only 2.5 V·cm. Moreover, the optimized STWEs, with a thickness of only 500 nm and a minimum linewidth of 5 μm, enable simplified fabrication and lower cost, making scalable ultra-high-speed modulator arrays possible.

II. Device Description

A. Device Model

Fig. 1 shows the schematic diagram of the TFLN modulator with STWEs. The optical unit is a conventional Mach–Zehnder interferometer (MZI) configuration, with a multimode interferometer (MMI) serving as the combiner. Edge couplers are employed at both the input and output ports to improve mode matching with standard optical fibers. The modulator employs an x-cut TFLN layer bonded onto a SiO_2 buffer grown on a high-resistivity silicon substrate. The TFLN layer is patterned into single-mode rib waveguides, which are further cladded with SiO_2 to reduce optical propagation loss as well as enhance EO interaction efficiency. The structural parameters of the LN rib waveguide and the thickness of the SiO_2 upper cladding will be discussed in Section III. An electric field is applied along the z-axis, allowing full exploitation of the largest EO coefficient r_{33} of the LN crystal. The electrical unit of the modulator is considered as a ground-signal-ground (G-S-G) configuration with STWEs, forming the CPW structure and naturally enabling push-pull modulation. Here, gold (Au) is considered as the electrode material due to the exceptionally low

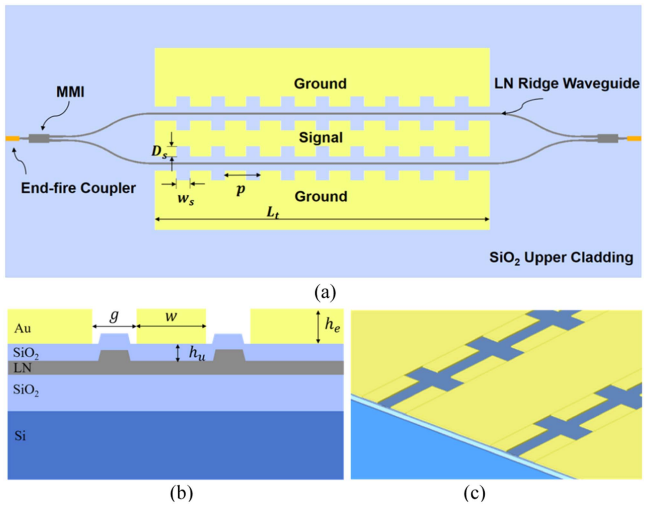

Fig. 1. (a) Top view, (b) cross-sectional view, and (c) three-dimensional schematic diagram of the TFLN modulator with STWEs.

surface resistance and small microwave loss, particularly at high frequencies beyond 200 GHz, as well as its excellent thermal and chemical stability. Compared with the normal straight-strip CPW electrode design, the sawtooth electrodes could offer more tunable structural parameters, including signal electrode width w, electrode thickness h_e, electrode gap g, sawtooth period p, as well as the width w_s and depth D_s of the air slot between adjacent teeth. Thus, more flexible and broad-band tunability could be obtained for optimizing the microwave characteristics of the transmission line. From a fabrication and cost-efficiency perspective, we aim to leverage the large feature size afforded by the sawtooth design, targeting relatively large w. Simultaneously, we would minimize h_e to lower metal consumption without compromising performance. The values of g, p, w_s, and D_s would determine the ultimate performance of the modulator and thus careful optimization is required.

To comprehensively assess the performance of the modulator, several key metrics are typically considered. First, the 3-dB bandwidth is defined as the frequency at which the EO response $H(f)$ drops by 3 dB from its DC value, serving as a direct indicator of high-speed modulation capability. $H(f)$ is given by [24]:

$$H(f) = 20\log_{10}\left|\frac{1}{L_t}\int_0^{L_t} H(f,z)dz\right|, H(f,z) = e^{(-\alpha+jb)z}, \tag{1}$$

where L_t is the length of the transmission line, $H(f, z)$ is the electrode transfer function, which primarily depends on the intrinsic parameters of the TWE. $H(f)$ can then be obtained by integrating $H(f, z)$ along z. The propagation of continuous-wave (CW) microwave signals is affected by certain losses and phase changes associated with the complex propagation constant for a certain frequency, which are reflected in the parameters α and b in the expression of $H(f, z)$. α is the microwave attenuation coefficient, and b is the velocity mismatch parameter between the optical and microwave signals, defined as:

$$b = \frac{2\pi f}{c_0}(n_p - n_g). \tag{2}$$

Here, n_p and n_g are the microwave phase refractive index and the optical group refractive index, respectively, and c_0 is the light speed in vacuum. Taking the reflection caused by the impedance mismatch at the input port into account, $H(f)$ can be calculated by:

$$H(f) = 20\log_{10} \times \left\{ \frac{2\sqrt{Z_0 Z_{in}}}{Z_0 + Z_{in}} e^{-\frac{\alpha L_t}{2}} \left[\frac{\sinh^2\left(\frac{\alpha L_t}{2}\right) + \sin^2\left(\frac{bL_t}{2}\right)}{\left(\frac{\alpha L_t}{2}\right)^2 + \left(\frac{bL_t}{2}\right)^2} \right]^{\frac{1}{2}} \right\}, \tag{3}$$

where Z_0 is the characteristic impedance of the transmission line, Z_{in} is the input impedance of the RF system, generally standardized at 50 Ω. The EO bandwidth is primarily determined by the velocity matching and microwave attenuation [5]. Specifically, the velocity matching refers to minimizing the difference between the microwave phase velocity in the electrodes and the optical group velocity in the waveguide, i.e., $n_p \approx n_g$. For electrodes without specific structural optimization, n_p is typically smaller than n_g. The microwave attenuation is quantified by the attenuation coefficient α, where lower values correspond to reduced microwave loss along the electrodes. Impedance matching is also crucial, requiring that the characteristic impedance Z_0 closely match the standard RF port impedance. Under ideal velocity-matched conditions ($n_p = n_g$, $b = 0$), the 3-dB EO bandwidth can be approximated by the 6.4-dB electrical bandwidth of the TWE.

Second, the half-wave voltage V_π refers to the voltage required to induce a π phase shift. A lower V_π, or smaller voltage-length product $V_\pi L_t$, indicates higher modulation efficiency and better device compactness. Lastly, the insertion loss, comprising coupling loss and on-chip transmission loss, plays a critical role in determining the overall energy efficiency and the optical link budget.

Based on these three key metrics that characterize the performance of modulator, the remaining parameters of the STWEs can be independently optimized. Concretely, electrode gap g is a critical determinant of V_π and the on-chip transmission loss, while sawtooth period p, slot width w_s, and depth D_s primarily influence the modulation bandwidth. Among these, D_s is particularly important, as it enables tuning of both the microwave loss and the microwave refractive index n_p, which are crucial to achieve larger 3-dB EO bandwidth and ultra-high-speed EO modulators. All structure parameters in the modulator would be optimized through simulations in Section III.

B. RGLC Model

The core modulation region of the modulator can be modeled as a transmission line, providing a reliable basis for optimizing the structural parameters that critically influence the device performance. The transmission line is an integrated electromagnetic system composed of the electrodes, surrounding dielectric materials, and the substrate, while the TWE serves as the core elements. The transmission line can be modeled by employing an RGLC lumped-element circuit, as shown in Fig. 2(a). The parameters R, G, L, and C represent the resistance, conductance, capacitance, and inductance per unit length of the conductors and dielectric, respectively. For brevity, the "per unit length" qualifier will be omitted in subsequent discussions. The values of these parameters are governed by the electrode geometry, the materials of the metal electrode and dielectric waveguide, all of which would determine the overall electromagnetic characteristics of the transmission line. Based on the RGLC model, the characteristic impedance Z_0 and complex propagation constant γ of the transmission line can be expressed as:

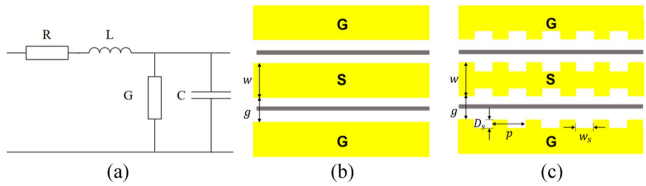

Fig. 2. (a) Equivalent circuit of the transmission line. (b) Straight-strip CPW electrodes. (c) STWEs.

TABLE I
RGLC MODEL PARAMETERS

Parameter	Unit	Expression
R	Ω/m	$R = \mathrm{Re}(Z_0\gamma)$
G	S / m	$G = \mathrm{Re}(\gamma / Z_0)$
L	μH / m	$L = \mathrm{Im}(Z_0\gamma)/\omega$
C	pF / m	$C = \mathrm{Im}(\gamma / Z_0)/\omega$

TABLE II
RF TRANSMISSION CHARACTERISTICS

Parameter	Unit	Expression
n_p	-	$n_p = c_0\sqrt{LC}$
α	Np/m	$\alpha \approx R/(2Z_0) + GZ_0/2$
Z_0	Ω	$Z_0 = \sqrt{L/C}$

$$Z_0 = \sqrt{\frac{R + j\omega L}{G + j\omega C}}, \tag{4}$$

$$\gamma = \sqrt{(R + j\omega L)(G + j\omega C)} = \alpha + j\beta \tag{5}$$

where α is the microwave attenuation coefficient with units of nepers per meter (Np/m) and β is the phase propagation constant with units of radians per meter (rad/m). The RGLC model parameters can be extracted from Z_0 and γ, as shown in Table I.

Under high-frequency and low-loss conditions, i.e., $R \ll \omega L$, $G \ll \omega C$, the microwave phase refractive index n_p, attenuation coefficient α, and characteristic impedance Z_0 can be further expressed by using the RGLC model parameters as shown in Table II.

The microwave refractive index n_p and characteristic impedance Z_0 of the transmission line are jointly determined by the inductance L and capacitance C. By properly tuning L and C, the microwave phase velocity and impedance can be

effectively manipulated, thereby enabling improved velocity and impedance matching. The microwave attenuation coefficient α is governed by both the conductor loss coefficient $R/(2Z_0)$ and the dielectric loss coefficient $GZ_0/2$. The former arises from the resistive energy dissipation due to the current flow in electrodes, which typically constitutes the dominant contribution, while the latter results from polarization-induced energy loss in the dielectric material. Optimizing the values of R, G, and Z_0 could minimize microwave propagation loss. A comprehensive tuning of the RGLC model parameters enables broader modulation bandwidth and more flexible control over the operating frequency of the modulator.

C. Equivalent Circuit Parameters of STWEs

In straight-strip CPW electrodes, the key tunable parameters are typically limited to the signal electrode width w and the electrode gap g, as shown in Fig. 2(b). This results in highly constrained control over the RGLC model parameters and poses challenges in resolving the intrinsic trade-off between half-wave voltage and bandwidth. To overcome this limitation, it is essential to increase the structural degrees of freedom, thereby enabling finer tuning of the RGLC model. The employed STWEs are shown in Fig. 2(c), which could increase the number of independently tunable structural parameters and thus provide additional structural degrees of freedom for performance optimization. The periodic rectangular features of the STWEs increase the effective length of the microwave transmission path, forming a slow-wave electrode structure that facilitates improved velocity matching. Moreover, the introduction of air slots would reduce the microwave loss. These periodic features also induce a meandering and elongated current path, which not only alters the current distribution and the spatial energy distribution of the electric field, but also enhances the local concentration of the magnetic field. As a result, the sensitivity of the RGLC model parameters to geometric variations is significantly increased so that the structure could be designed more flexibly.

Given the periodicity of STWEs, each elementary unit comprises a rectangular metal tooth and an adjoining rectangular air slot oriented in the signal transmission direction. When the sawtooth period p is not particularly small (especially in our design with large-size electrodes) the electromagnetic interactions between adjacent unit cells can be neglected. This assumption will be validated in the subsequent analysis of the RGLC model parameters for the STWEs. In this regime, the RGLC model parameters of a single STWEs unit cell are theoretically equivalent to those of the entire transmission line, and p can be considered equivalent to the transmission line length and treated as a fixed parameter, since its variation does not affect the field distribution within the unit cell. Therefore, we can perform a quantitative analysis on a single electrode unit cell at a fixed microwave frequency to investigate how the RGLC model parameters vary with the slot width w_s and depth D_s.

1) Resistance: We begin with the resistance of STWEs. The fundamental definition is $R = \rho l/S$, where ρ is the resistivity of the electrode material, l is the length of the current path and S is the effective cross-sectional area through which the current flows. For metallic electrodes, the effective cross-sectional area S must account for both the skin depth and the equivalent electrode width. Accordingly, R can be expressed as:

$$R \approx \frac{\rho}{h_{eff}} \frac{p+2d_s}{pw-2w_s d_s} \left(h_{eff} = \int_0^{h_e} J(\delta)dx, \delta = \sqrt{2\rho/\omega\mu} \right), \tag{6}$$

where ρ is the resistivity of the electrode material, h_e is the electrode thickness, h_{eff} is the effective height of the cross section. h_{eff} is obtained by integrating the actual current distribution $J(\delta)$ along the vertical direction x, where $J(\delta)$ typically follows an exponential decay profile and δ is the skin depth calculated by ρ, microwave signal angular frequency ω and magnetic permeability μ of the electrode material. The product of h_{eff} and the calculated equivalent width $pw-2w_sD_s$ of the signal electrode yields the effective cross-sectional area for uniform current flow. Since w_sD_s is typically one order of magnitude smaller than pw, the variation of R induced by the slot width w_s can be neglected. Therefore, R can be regarded as a function of the slot depth D_s. By performing a Taylor expansion of R at $D_s = 0$, the resulting Taylor polynomial is given by:

$$R = \frac{\rho}{h_{eff}w} \left(1 + \sum_{i=1}^{\infty} A_i {D_s}^i \right). \tag{7}$$

Since D_s is relatively small compared to signal electrode width w and sawtooth period p, the Taylor expansion can be approximated. The conditions for the validity of first- and second-order approximations of D_s are:

$$\frac{A_2{D_s}^2 + A_3{D_s}^3}{1 + A_1D_s} \le \varepsilon_{tol}, \frac{A_3{D_s}^3}{1 + A_1D_s + A_2{D_s}^2} \le \varepsilon_{tol}. \tag{8}$$

ε_{tol} represents the error tolerance. $A_i (i = 1, 2, 3)$ are the coefficients of the ${D_s}^i$ terms, which depend on w and p, and are given by:

$$A_1 = \frac{2}{p}\left(1 + \frac{w_s}{w}\right), A_2 = \frac{4w_s}{p^2w}\left(1 + \frac{w_s}{w}\right),$$
$$A_3 = \frac{8{w_s}^2}{p^3w^2}\left(1 + \frac{w_s}{w}\right). \tag{9}$$

As D_s increases, the current path becomes more tortuous and the conductive channel continuously narrows, leading to a significant increase in local current density. Consequently, R may exhibit accelerated growing behavior, making higher-order terms in the Taylor expansion non-negligible. The appropriate truncation order of the expansion depends on specific structural parameters.

2) Conductance: The conductance of STWEs is primarily determined by the electric field distribution within the dielectric material, which can be expressed by the field-theoretic expression:

$$G \sim \omega\varepsilon_0 \int_V |E_{local}|^2 \tan\delta dV, \tag{10}$$

where ω is the angular frequency of the signal, ε_0 is the vacuum permittivity, $|E_{local}|^2$ is the local electric field intensity distribution within the dielectric, and $\tan\delta$ is defined by the ratio of the imaginary to the real part of the permittivity of the

materials. Since the variation of $\tan\delta$ is much smaller than that of $|E_{local}|^2$, the fluctuations of G are mainly controlled by the local electric field. G is particularly sensitive to localized field enhancements and nonlinear field modulations introduced by the sawtooth geometry. Such modulations can lead to strong spatial inhomogeneity in the dielectric loss distribution, especially near sharp features or high curvature regions of the electrode profile. When the geometric parameters of STWEs (e.g., the slot depth D_s and width w_s) change, the spatial distribution of the electric field changes accordingly, leading to non-monotonic variations of G and making analytical prediction challenging. Consequently, numerical simulations have to be employed to obtain the complex interplay between geometry-induced field distortion and the corresponding dielectric response.

3) Inductance: The inductance of STWEs can be considered as comprising two components. The dominant contribution to the inductance arises from the magnetic field confined between the signal and ground electrodes with a spacing g, and can be approximated by the inductance of the straight-strip CPW electrodes with the same spacing, denoted as L_0. The secondary contribution originates from the magnetic field within the rectangular air slot. Assuming uniform magnetic field distributions in both regions and a relative field strength ratio of r, the inductance can be estimated based on the definition $L = \Phi/I$, where Φ is the magnetic flux associated with the current loop and I is the current through the conductor.

We begin by fixing the slot width w_s and exploring the relation between L and the slot depth D_s. Theoretically, when D_s varies, the structure along the propagation direction remains unchanged, resulting in minimal disturbance to the magnetic field distribution. Hence, the nonlinear magnetic response can be neglected, and Φ can be assumed to be directly related to the uniform magnetic field strength and the current loop area. To validate this, we construct HFSS models of STWEs with varying D_s, and plot the surface current paths and magnetic field distributions, as shown in Fig. 3(a) and (b). As D_s increases, the surface current paths would increase accordingly. The magnetic field is predominantly distributed in the region between the signal and ground electrodes, leading to field enhancement at the edges of the electrodes. It can be seen that the magnetic field near the edges of the air slots remains nearly uniform and constant across different D_s, indicating a stable and uniform field distribution within the slots. Meanwhile, the transverse magnetic field distributions exhibit high stability with varying D_s. In this case, Φ increases linearly with D_s, and L can be expressed as:

$$L \approx L_0 + Bw_sD_s, B = \frac{2rL_0}{pg}, \tag{11}$$

where the coefficient a depends on the magnetic field strength ratio r, the inductance L_0 of conventional electrodes, the sawtooth period p and the electrode gap g. L_0 and B are constants when other structural parameters are held fixed, indicating a linear dependence of L on D_s.

In contrast, when D_s is fixed and w_s is varied, the lateral boundary conditions are altered. In particular, the alternation between metal teeth and air slots may cause field lines to jump or reconfigure, leading to localized enhancement or reduction of the magnetic flux. Fig. 3(c) and (d) show the surface current paths and magnetic field distributions of the STWEs under different w_s. It can be observed that although the surface current path length remains nearly unchanged with varying w_s, the transverse magnetic field undergoes a redistribution, especially in the air slot region highlighted by the red ellipse. As a result, the field strength can no longer be approximated as constant. Under these conditions, the coefficients L_0 and B in (11) would depend on w_s. To account for these effects, we introduce a fluctuation term $\varepsilon_L(w_s)$ to modify (10), yielding the complete expression L:

$$L \approx L_0 + Bw_sD_s + \varepsilon_L(w_s), B = \frac{2rL_0}{pg}. \tag{12}$$

4) Capacitance: The fundamental definition of capacitance is $C = Q/V$, where Q is the total stored charge and V is the potential difference between the signal and ground electrodes. In CPW structure, the charge distribution is predominantly concentrated along the edges and surfaces of the electrodes adjacent to the gap region between electrodes. The region of charge accumulation is defined as the effective coupling area A_{eff}. We constructed STWEs models in HFSS by varying the slot depth D_s and width w_s, respectively, and the corresponding electric field distributions are shown in Fig. 4(a) and (b). In Fig. 4(a), the transverse electric field on the tooth surface is uniformly distributed, while the longitudinal electric field is concentrated at the edges of the teeth, forming the effective coupling region. Within approximately 2 μm from the tooth edge, a high-intensity field region is observed, beyond which the field intensity drops sharply, creating a discontinuity. The air slots of STWEs reduce the charge within this effective coupling region. As D_s increases, a larger portion of charge becomes non-contributing, as indicated by the red ellipse in Fig. 4(a). In our design, the electrodes have relatively large dimensions with D_s values typically greater than

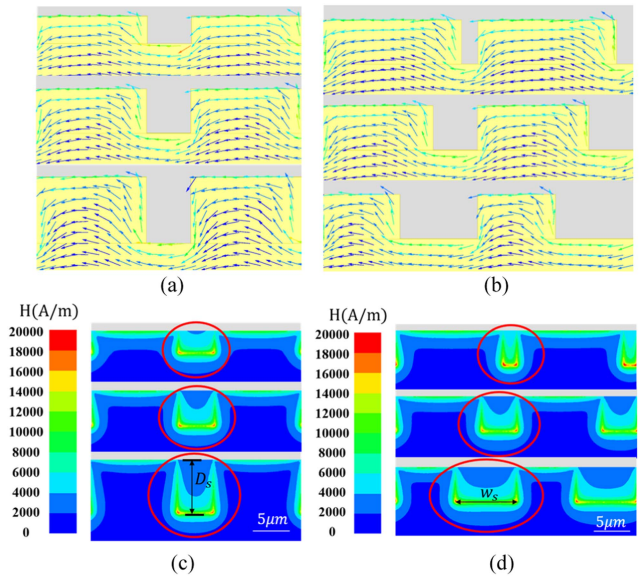

Fig. 3. (a) Surface current paths and (b) magnetic field distributions for different D_s (5 μm, 8 μm and 12 μm) on the STWEs with $w_s/p = 0.3$. (c) Surface current paths and (d) magnetic field distributions for different w_s/p (0.1, 0.3, 0.5) on the STWEs with $D_s = 8$ μm.

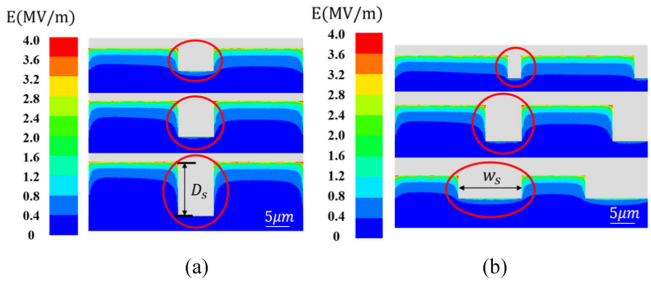

Fig. 4. (a) Electric field distributions for different D_s (5 μm, 8 μm and 12 μm). (b) Electric field distributions for different w_s/p (0.1, 0.3, 0.5), $D_s = 8$ μm.

2 μm, which implies that the high-field region near the edge can be effectively disregarded. As a result, the total stored charge decreases approximately linearly with D_s. Therefore, C can be approximated as:

$$C \approx C_0 - kw_sD_s, k = \frac{2C_0}{A_{eff}}, \tag{13}$$

where C_0 is the capacitance of the straight-strip CPW electrodes with the same gap spacing as STWEs, and the coefficient k quantifies the sensitivity of the capacitance to the slot geometry, depending on C_0 and the effective coupling area A_{eff}. C_0 and k are constants when other structural parameters are held fixed. This linear approximation provides a first-order model for the impact of slot-induced charge depletion on the overall capacitance.

As with the analysis of L, the influence of w_s on C is complex. Variations in w_s would not only affect the amount of charge reduced by the air slots but also vary the spatial distribution of the electric field along the propagation direction and modify the effective coupling area A_{eff}, potentially leading to modal field hopping and abrupt non-linear changes in energy distribution. As shown in Fig. 4(b), the air slot region is marked by the red ellipse. Increasing w_s causes more electric field energy to leak toward the edges of the air slots, thereby reshaping the transverse field distribution. This necessitates the introduction of a fluctuation term $\varepsilon_C(w_s)$ to modify (13). Consequently, the final expression for C can be expressed as:

$$C \approx C_0 - kw_sD_s + \varepsilon_C(w_s), k = \frac{2C_0}{A_{eff}}. \tag{14}$$

Moreover, it can be found that the magnetic and electric field distributions shown in Figs. 3(d) and 4(b) for two adjacent electrode unit cells exhibit high consistency. It confirmed the effectiveness of the utilized unit-cell-based approach to simplify the analysis of the transmission line.

Based on the above analysis, the slot depth D_s is identified as a key parameter that determines the RGLC model of the STWEs. R can be expressed as a polynomial function of D_s, while L and C exhibit approximately linear but opposite trends with respect to D_s. According to the expressions of the microwave refractive index n_p and the microwave attenuation coefficient α provided in Table II, there exists a specific range of D_s in which n_p reaches either a maximum value or becomes closest to n_g, while α attains a minimum. Our objective is to identify a value of D_s that enables both optimal velocity matching and minimal microwave loss through simulation-based optimization. Before this, it is necessary to determine reasonable values for sawtooth period p and the slot width w_s to ensure stable electromagnetic wave propagation to the output port without excessive microwave reflection within the structure, while minimizing microwave loss.

III. Simulation and Optimization

The modulator utilizes x-cut TFLN with a thickness of 400 nm, bonded on a 2-μm-thick SiO_2 layer grown on a high-resistivity silicon substrate. Based on the single-mode transmission condition, the waveguide has a top width of 1 μm and an etch depth of 200 nm. The transverse electric (TE) mode optical field distribution is simulated by Lumerical MODE Solutions, as shown in Fig. 4(a). The mode is well confined within the etched waveguide region. The group refractive index of the optical mode is found to be $n_g = 2.22$. It should be noted that the wavelength range considered in this study is approximately 1530–1565 nm (C-band), and the group refractive index within such range is 2.22 ± 0.0025 according to the simulation results. Thus, the impact of the group refractive index on the modulator bandwidth is negligible. The electrostatic field distribution between the STWEs is simulated by COMSOL Multiphysics, as illustrated in Fig. 4(b). It can be seen that the electric field is strongest near the electrode edges and effectively overlaps with the LN waveguide, enabling efficient refractive index modulation. The modulation efficiency, characterized by half-wave voltage V_π, is primarily determined by the SiO_2 upper cladding thickness h_u and the electrode gap g. A thicker cladding layer or a wider electrode gap would reduce the optical propagation loss caused by metal absorption. However, both configurations would weaken the overlap between the optical and electric fields, resulting in a larger V_π or voltage-length product $V_\pi L_t$. Thus, there is a trade-off between minimizing optical loss and maximizing modulation efficiency. $V_\pi L_t$ and the optical propagation loss of LN ridge waveguide can be estimated using the following expression:

$$V_\pi L_t = \frac{n_{eff}\lambda g}{2{n_e}^4 r_{33}\Gamma}, \tag{15}$$

$$Loss = abs\left(\frac{40\pi}{\ln(10)\,\lambda}\mathrm{Im}(n_{eff})\right), \tag{16}$$

where n_{eff} is the effective index of the optical mode, λ is the operation wavelength of the optical signal, n_e is the extraordinary refractive index of LN, r_{33} is the EO coefficient of LN along the z-axis, and Γ represents the overlap integral between the optical and electric fields. Parameters including n_{eff}, n_e, and Γ can be extracted through COMSOL Multiphysics simulations.

To obtain the proper value for h_u and g, the optical loss and $V_\pi L_t$ need to be calculated for a wide range of combinations of these two values. We have simulated them with various structural parameters, where h_u ranged from 0 to 500 nm and g spanned 3–8 μm. As shown in Fig. 5(c), $V_\pi L_t$ exhibits a positive correlation with both h_u and g. The reason is that the increased SiO_2 thickness in the waveguide structure would

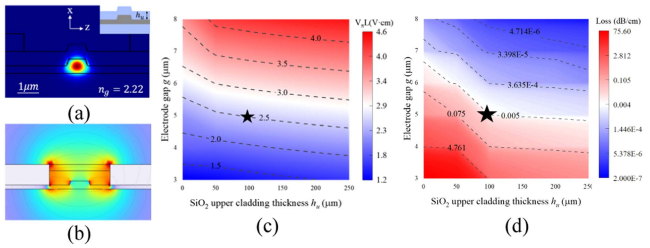

Fig. 5. (a) The optical field of the transverse electric (TE) mode. (b) The electrostatic field of STWEs. (c) Two-dimensional colormap plot of the $V_\pi L_t$ (d) and optical loss versus different gaps g and upper cladding thickness h_u.

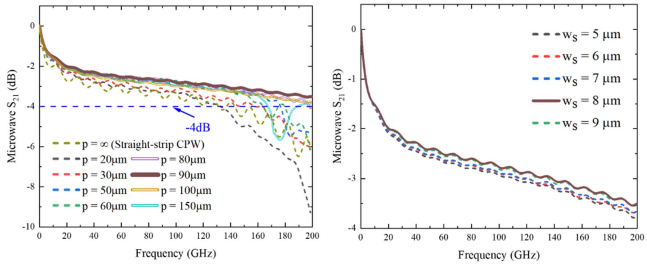

Fig. 6. Simulated microwave S_{21} of the STWEs with (a) different sawtooth period p ($D_s = 9$ μm, $w_s/p = 0.1$) and (b) different slot width w_s ($D_s = 9$ μm, $p = 90$ μm).

weaken the electric field interaction with the LN, necessitating higher driving voltages for effective modulation. Larger electrode spacing reduces the inter-electrode electric field intensity, thereby decreasing the optical modulation efficiency. In contrast, h_u and g exhibit an opposite influence on optical loss, as shown in Fig. 5(d), which presents the propagation loss in dB/cm. This inherent trade-off between low $V_\pi L_t$ and low propagation loss requires careful parameter optimization. Considering practical fabrication constraints, particularly photolithographic alignment challenges, we selected $h_u = 100$ nm and $g = 5$ μm (marked by pentagrams in Fig. 5(c)–(d)). Under such arrangement, the $V_\pi L_t$ is approximately 2.5 V·cm while maintaining an exceptionally low electrode absorption loss of 0.005 dB/cm, which can be neglected. Based on our design at the wavelength of 1550 nm, the loss introduced by a single MMI is approximately 0.5 dB, the coupling loss is about 0.5 dB per facet, and the empirical transmission loss during fabrication is 0.2 dB/cm. Therefore, the total insertion loss of the modulator is estimated to be ∼2.4 dB.

The RF properties of the STWEs were simulated through HFSS. As discussed in Section II, our aim is to design the electrodes with relatively wide width and thin thickness. Therefore, the STWEs is designed as a signal electrode width w of 45 μm and a thickness of 500 nm. The arm length L_t of the MZI is set to be 5 mm. Before optimizing the slot depth D_s to achieve both optimal velocity matching and minimal microwave loss, the sawtooth period p and the slot width w_s should be optimized at first. In theory, the field distribution inside each STWEs unit cell remains unaffected by p. However, if p is too large, the sawtooth would become too sparse within a fixed modulation length, thereby diminishing the effectiveness of geometric modulation on the RGLC parameters. Conversely, if p is too small, the metal edges would be too dense, which may lead to magnetic field crosstalk between adjacent slots. It would not only increase microwave loss but also increase the fabrication complexity and cost. We have simulated the STWEs with different p ranging from 20 μm to 150 μm and extracted the transmission coefficient S_{21} to evaluate the microwave transmission performance, as shown in Fig. 6(a). For comparison, we also simulated the straight-strip CPW electrodes, which can be regarded as the limiting case where $p = \infty$. When $p = 20$ μm, the microwave transmission is even worse than that of the straight-strip CPW electrodes, indicating that the metal teeth are too densely packed. It leads to frequent geometric discontinuities, which enhance microwave reflections between adjacent teeth and hinder efficient propagation. For $p = 30$, 50, and 60 μm, the structural perturbation still introduces noticeable microwave reflection, particularly in the high frequency range of 160–200 GHz. The S_{21} curves for these cases are plotted as dashed lines. When the period increases to 80, 90, and 100 μm, S_{21} remains above -4 dB, with the best performance observed at $p = 90$ μm, indicating stable and low-loss microwave transmission. However, further increasing p to 150 μm results in noticeable degradation around 180 GHz, suggesting that the periodic modulation becomes too weak to effectively tailor the RGLC model parameters. Therefore, $p = 90$ μm is identified as the optimal sawtooth period for achieving high transmission performance.

The slot width w_s plays a critical role in determining the modulation efficiency of the device. If w_s is too large, the air slot would occupy too much of one period so that the modulation efficiency would be degraded. Since the electric field in the air slots is very weak, its impact on the V_π is generally considered negligible when the duty cycle is below 10%. Conversely, if w_s is too small, the magnetic field tends to localize near the slot edges, leading to thermal accumulation. Moreover, a narrower slot would also increase the fabrication complexity. Therefore, w_s is chosen within the range of 5–9 μm for a period $p = 90$ μm. Given the narrow variation range of w_s, the induced fluctuations in L and C are negligible. Thus, we directly examine the transmission coefficient S_{21} to identify the optimal value of w_s that minimizes microwave loss. The simulated microwave S_{21} for $w_s = 5$–9 μm (step = 1 μm) are shown in Fig. 6(b). The best performance is achieved at $w_s = 8$ μm, which is therefore selected as the optimal slot width.

The slot depth D_s serves as the key parameter in determining the RGLC model of the STWEs. An excessively large D_s substantially increases the current path length, leading to higher ohmic losses. Conversely, if the slot is too shallow, the current concentration near the slot edges cannot be avoided, which violates the assumptions of the established RGLC model and also poses challenges for device fabrication. With a signal electrode width of 45 μm, D_s is considered within the range of 5–9 μm, with a step size of 0.5 μm. Then, TFLN modulator models are considered at four representative microwave frequencies: $f = 50$, 100, 150, and 200 GHz. We first focus on optimizing the velocity matching. According to$n_p = c_0\sqrt{LC}$, we extract the L and C, as shown in Fig. 7(a) and (b), respectively. The results

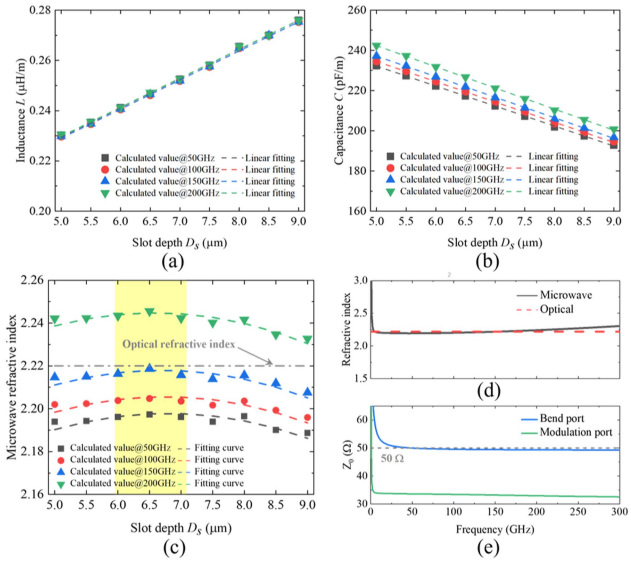

Fig. 7. Variation of (a) the inductance L, (b) the capacitance C, and (c) the microwave refractive index with slot depth D_s. (d) Simulated microwave refractive index at $D_s = 6.5$ μm, and optical refractive index. (e) Simulated characteristic impedance Z_0 of the bend and modulation section ports at $D_s = 6.5$ μm.

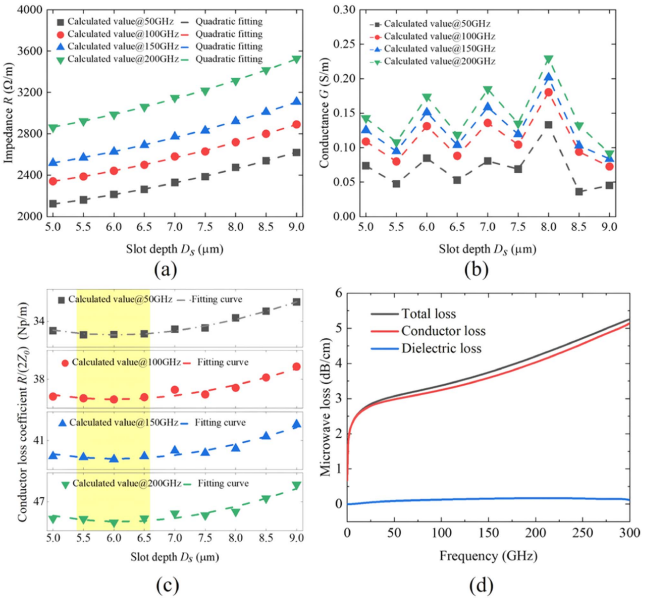

Fig. 8. Variation of (a) the resistance R, (b) the conductance G, and (c) the conductor loss coefficient $R/(2Z_0)$ with slot depth D_s; (d) Calculated total microwave loss, conductor loss, and dielectric loss at $D_s = 6.5$ μm.

indicate that L increases linearly with D_s, which can be well-fitted by a line with a positive slope. Conversely, C decreases linearly with increasing D_s, which can be fitted by a line with a negative slope. These trends are consistent with our theoretical predictions. Notably, this linear relation persists across multiple frequencies, demonstrating the robustness of our analysis over a broad microwave bandwidth. Based on the fitted values of L and C, we calculated the actual and fitted values of the microwave refractive index, as shown in Fig. 7(c). The microwave refractive index initially increases and then decreases with increasing D_s. To achieve high EO bandwidth, velocity matching at relatively low frequencies (below 150 GHz) is prioritized. Therefore, the range of $D_s = 6$–7 μm is considered as the optimal interval. Taking $D_s = 6.5$ μm as an example, the frequency-dependent curves of microwave and optical refractive indices, as well as the characteristic impedance Z_0, are shown in Fig. 7(d) and (e). Nearly perfect velocity matching is achieved across the entire 0–300 GHz bandwidth ($n_g = 2.22$). The characteristic impedance of the modulation section port is approximately 34 Ω, which deviates from the standard 50 Ω impedance commonly used in RF systems. In practical device designs, a bend section is typically introduced to route the electrode terminals onto a separate plane, enabling independent electrical and optical probing. Therefore, it is sufficient to achieve impedance matching only at the bend section port. As shown in Fig. 7(e), a characteristic impedance of 50 Ω is achieved by designing the electrode gap in the bend section as 50 μm and the signal electrode width as 50 μm, thereby ensuring perfect impedance matching. The schematic diagram of the bend section port and modulation section port are shown in Fig. 9(a).

Based on the previous theoretical analysis, the relation between R and the slot depth D_s can be expressed by (7). The conditions for first- and second-order Taylor approximations

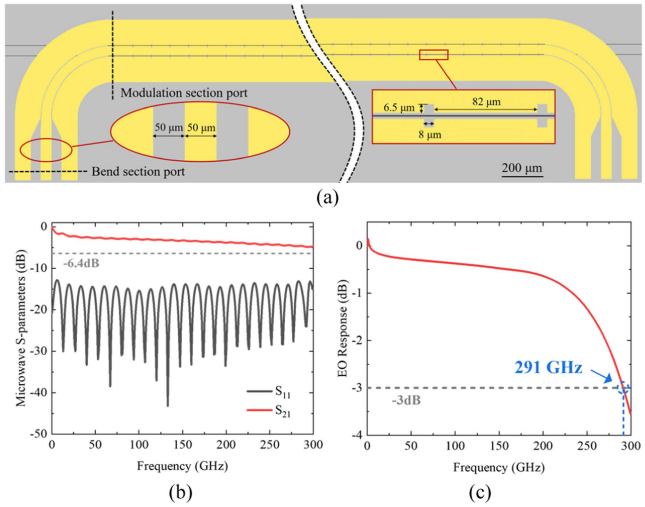

Fig. 9. (a) Schematic diagram of the complete TFLN modulator with the optimized STWEs ($L_t = 5$ mm). (b) Simulated microwave S-parameters and (c) calculated EO response of the modulator.

are (8) and (9). By setting the error tolerance ε_{tol} to 0.5% and substituting the optimized values of signal electrode width w, sawtooth period p, and slot width w_s, we find that the conditions for the validity of the first- and second-order approximations are $D_s \leq 7.38$ μm and $D_s \leq 21.53$ μm, respectively. This confirms that (7) can be approximated up to the second order as:

$$R = \frac{\rho}{HW}\left(1 + A_1 D_s + A_2 {D_s}^2\right) \tag{17}$$

Fig. 8(a) shows the variation of R with D_s at 50, 100, 150, and 200 GHz. It is observed that R increases nonlinearly with D_s, and the data can be accurately fitted by a quadratic function, in good agreement with our theoretical prediction. This fitting

behavior remains robust across different f. As shown in Fig. 8(b), with increasing slot depth D_s, the fluctuation amplitude of the conductance G increases. The reason is that a larger slot depth would enhance the local electric field concentration at the slot bottom and the sharp edges of the slot walls, resulting in a more complex spatial distribution of the local electric field $|E_{local}|^2$. Meanwhile, the microwave field inside the slot produces local interference, which further increases the fluctuation amplitude of the integral value. This observation is consistent with the analysis in Section II-C-2 regarding the origin of G fluctuations. We also note that G would increase with the microwave signal frequency, consistent with (10). These results further refine the RGLC model of the STWEs, indicating that the non-monotonic behavior of G arises from the increased complexity of the local electric field distribution due to geometric parameter variations, rather than from simulation noise.

As previously discussed, the conductor loss dominates the total microwave attenuation and is key to reducing overall microwave loss. The actual and fitted values of the conductor loss coefficient $R/(2Z_0)$ as a function of D_s are plotted in Fig. 8(c). With increasing D_s, the conductor loss initially decreases and then increases, reaching a minimum around $D_s = 5.5$–6.5 μm across all simulated frequencies. Therefore, selecting $D_s = 6.5$ μm enables simultaneous optimization of velocity matching and microwave attenuation, leading to enhanced EO bandwidth performance of the modulator. Fig. 8(d) further illustrates the frequency-dependent behavior of the total microwave loss, conductor loss and dielectric loss at $D_s = 6.5$ μm. Simulation results indicate that the total microwave loss remains below 5.5 dB/cm at 300 GHz. The dielectric loss stays below 0.2 dB/cm across the 0–300 GHz frequency range and is negligible compared to the conductor loss, thereby validating the rationale of focusing the optimization on conductor loss alone.

Then, we constructed the TFLN modulator model with the optimized STWEs and performed simulations to obtain the microwave S-parameters, as shown in Fig. 9. Fig. 9(a) shows the complete TFLN modulator with optimized STWEs, including the modulation and bend sections. The radius of the arc that connects to the signal electrode is 300 μm. It is noted that the electrodes directly cover the waveguide in the bend regions, which could lead to significant optical absorption. Therefore, the SiO_2 upper cladding in the bend regions is designed to be 1 μm thick, while the modulation region has a thinner cladding of 100 nm. During fabrication, an electrode ramping process is applied, which can be realized by controlling the etching angle of the SiO_2. Under this design, the absorption loss induced by the metal electrodes can be considered negligible. Within the 0–300 GHz frequency range, the return loss S_{11} remains below –10 dB, satisfying the impedance matching requirement. The simulated transmission coefficient S_{21} accounts for both impedance matching and microwave attenuation. As shown in Fig. 9(b), S_{21} is better than -6.4 dB across the entire band, theoretically supporting a 6.4-dB electrical bandwidth over 300 GHz. Based on all the results, the EO modulation response can be calculated using (3), which takes the effects of slight velocity mismatch and impedance mismatch into consideration. The calculated 3-dB EO bandwidth can be as high as 291 GHz, as shown in Fig. 9(c). Table III lists the performance metrics of TFLN modulators with existing mainstream electrode designs at a light wavelength of 1550 nm, including EO bandwidth and $V_\pi L_t$. It can be seen that our design exhibits a significant advantage in EO bandwidth, which is attributed to the analytical expressions linking the RGLC model with the electrode structural parameters, while simultaneously achieving optimal velocity matching and minimal microwave loss. The results in the table could validate the effectiveness of our optimization method.

TABLE III
PERFORMANCE COMPARISON OF TFLN MODULATORS WITH RECENT MAINSTREAM ELECTRODE DESIGNS

Electrode design	EO bandwidth (GHz)	$V_\pi L_t$ (V·cm)
Straight-strip[12]	>50	2.9
Straight-strip[25]	>40	1.75
Straight-strip[26]	>40	1.29
Straight-strip[27]	60	2.7
CL-TWEs[20]	>67	2.6
CL-TWEs[21]	>70	2.1
CL-TWEs[14]	120	2.5
CL-TWEs[15]	160	1.62
CL-TWEs[17]	218	1.33
STWEs[23]	>110	3.1
STWEs (This work)	290	2.5

IV. DISCUSSIONS

A. Extension to Arbitrary Periodic Electrodes

In this work, we take the STWEs as an example to demonstrate an optimization method for TWEs based on the RGLC equivalent transmission line model. This method relies on the fundamental definitions of the circuit parameters to analyze the electromagnetic field evolution, and is general and independent of the specific metal or dielectric materials utilized. Moreover, this optimization method is not restricted to STWEs. It can be extended to a broad class of CPW electrodes with periodic structural features. Taking CL-TWEs as an example, the effective geometric parameters of the CL-TWE unit cell, including the length, width, duty cycle, and spacing of the T-rails, are determined at first. By simulating the electric field within the unit cell structure, the analytical relation between the RGLC parameters and geometric parameters can be derived, which is similar to the procedure of determining the sensitivity of RGLC parameters to geometric features in STWE units. Subsequently, numerical simulations can be performed in HFSS to adjust the distributed C and L for velocity matching, while controlling R and G to minimize electrode loss. Through fine-tuning of geometric parameters, a bandwidth enhancement can be realized as that achieved in this work. This generality enables rapid parametric exploration and physical insight into how electrode geometry influences signal propagation characteristics, thus

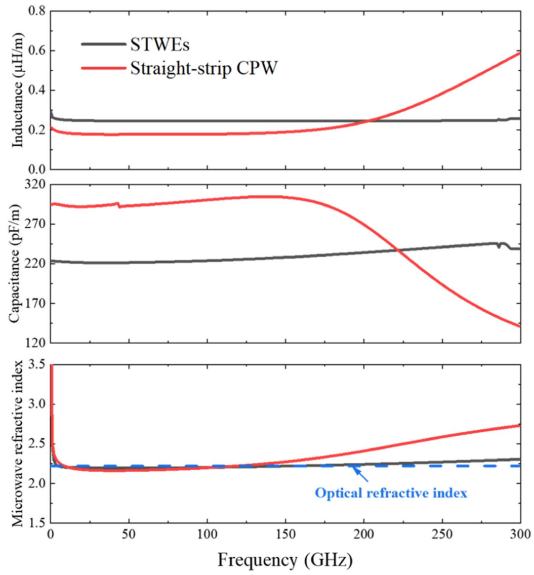

Fig. 10. Comparison of the simulated inductance, capacitance, and microwave refractive index between the STWEs and the straight-strip CPW.

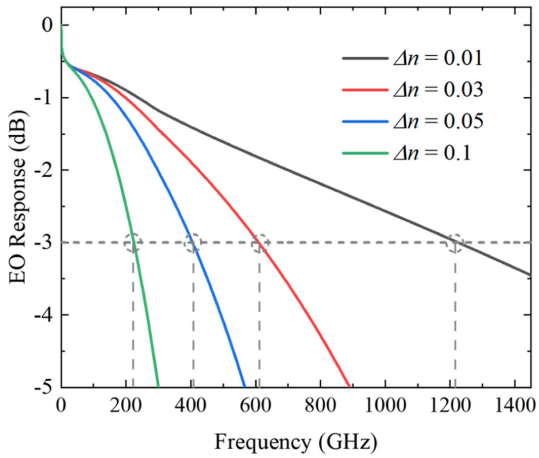

Fig. 11. Calculated EO response of the 5 mm long modulator with the optimized STWEs when $\Delta n = 0.01$, 0.03, 0.05, and 0.1.

offering a powerful tool for the design of high-performance EO modulators across a wide frequency range.

B. How to Achieve Larger EO Bandwidth

The linear EO effect (Pockels effect) in LN involves no participation of free carriers and exhibits a femtosecond-scale response time. As a result, the intrinsic bandwidth of TFLN modulators is not limited by the material itself, but rather by the device structure [28]. Velocity mismatch between microwave and optical signals is the primary bandwidth-limiting mechanism in EO modulators and is particularly critical for achieving ultra-high-speed operation [29]. In straight-strip CPW electrodes, significant velocity mismatch emerges at high frequencies, leading to a rapid roll-off in modulation response. The STWEs address this challenge through geometric loading and control of inductance and capacitance, which suppresses the increase in microwave effective index at high frequencies. Fig. 10 compares the unit-length inductance L, capacitance C, and microwave refractive index of the two electrode types. As shown, for microwave frequencies above 150 GHz, straight-strip CPW electrodes exhibit a sharp increase in L due to the skin effect and current crowding at the conductor edges. Meanwhile, the electric field in the straight geometry spreads and leaks significantly at high frequencies, resulting in a rapid decrease in C, which causes the microwave index to deviate from the target value. In contrast, the optimized STWEs alleviate current crowding through tailored geometry, thereby flattening the frequency dependence of L. At the same time, local field enhancement in the air slots helps to confine the field and enhance energy storage, leading to a stable capacitance. As a result, both L and C remain nearly constant across the 0–300 GHz band, effectively suppressing the increase in microwave index.

However, it should be noted that velocity matching in the STWEs would be deteriorated at frequencies above 200 GHz ($\Delta n = n_p - n_g > 0.02$), and reaches approximately $\Delta n \approx 0.08$ at 300 GHz. It is attributed to the rise in capacitance caused by local electric field enhancement. The increase in Δn beyond 200 GHz corresponds well with the accelerated decline in EO response observed in Fig. 9(b), providing preliminary evidence that velocity matching plays a critical role in determining modulation bandwidth. To further evaluate the impact of velocity mismatch on modulation bandwidth, we consider an idealized scenario where microwave loss and impedance mismatch are neglected. Under this assumption, the theoretical bandwidth limit of a TFLN modulator can be expressed by [29] :

$$H(f) = \frac{2c_0}{\pi \Delta n L_t}. \tag{18}$$

Assuming perfect velocity matching ($\Delta n = n_p - n_g = 0.01$) and a modulation length $L_t = 5$ mm, the maximum achievable bandwidth is calculated to be 3.8 THz. However, in practical devices, microwave loss is inherently present, and slight impedance mismatch is inevitable due to fabrication tolerances. Therefore, we further analyze the EO response of the designed TFLN modulator under various Δn conditions (0.01, 0.03, 0.05, and 0.1), taking microwave loss and impedance mismatch into account. Given that our design has already minimized microwave loss and optimized impedance matching, using the simulation results from this work provides a reasonable and representative assessment of bandwidth performance under realistic operating conditions. The simulation results are shown in Fig. 11. When velocity matching is perfect ($\Delta n = 0.01$), the modulator can achieve a terahertz-level bandwidth (>1.2 THz). When Δn increases to 0.03, 0.05, and 0.1, the corresponding bandwidths significantly drop to approximately 600 GHz, 400 GHz, and 200 GHz, respectively, which highlights the substantial impact of velocity mismatch on bandwidth performance. Notably, the relation between Δn and bandwidth degradation is nonlinear. The most pronounced deterioration occurs as Δn increases from 0.01 to 0.03, while further increases in Δn result in progressively smaller reductions in bandwidth. This trend indicates that the modulation bandwidth is particularly

sensitive to small deviations in Δn. Therefore, in the design of ultra-high-speed EO modulators, it is essential to meticulously control Δn to maximize the achievable bandwidth.

To achieve a stable per-unit-length capacitance across a wide frequency range (e.g., 0–300 GHz), we can consider optimizing the substrate configuration and electrode material selection. Previous studies on CL-TWEs have shown that introducing a low-permittivity buffer layer between the electrodes and the substrate helps achieve velocity matching. Inspired by this approach, a similar low-k dielectric, such as thickened SiO_2 [30], BCB [19], or fluorinated polymers, can be introduced beneath the electrodes to stabilize the electrostatic field distribution and reduce capacitance variation over a broad frequency spectrum. In addition, increasing the electrode metal thickness helps to confine the current distribution and maintain quasi-TEM mode propagation, which improves the high-frequency stability of the capacitance. The current metal thickness is only 500 nm; increasing it to 1–2 μm is compatible with the present electrode design. However, for large-scale modulator arrays, the cost associated with thick gold electrodes can be prohibitive. As a trade-off, low-cost alternatives such as copper [31] or aluminum [12] may be considered, provided that suitable passivation or diffusion barrier layers (e.g., TiN, TaN [32]) are applied to ensure long-term device reliability. These approaches are currently under investigation in our ongoing work.

C. Bandwidth-Length Trade-Off

The modulation arm length L_t is one of the key parameters influencing the EO bandwidth of modulators. In TWE based EO modulators, the modulation efficiency increases proportionally with L_t, while the bandwidth tends to decrease with increasing length. This is primarily due to enhanced conductor loss and cumulative velocity mismatch effects along longer propagation distances. In this work, we systematically investigate the impact of different L_t values (5, 7, and 10 mm) on the 3-dB EO bandwidth through numerical simulations, as shown in Fig. 12. The results reveal that increasing the modulation length to 7 mm reduces the bandwidth to 262 GHz, while further increasing to 10 mm results in a bandwidth of 234 GHz. This trend highlights the intrinsic inverse relations between bandwidth and modulation length and confirms that longer electrodes weaken high-frequency modulation performance. Nonetheless, it is noteworthy that even with a modulation length up to 10 mm, the EO bandwidth remains above 200 GHz, which validates the effectiveness of our optimized STWEs design.

Although larger L_t can improve modulation depth and reduce the half-wave voltage V_π, it imposes greater limitations on system bandwidth, especially in the high-frequency regime beyond 200 GHz. For applications targeting terahertz-speed modulation, blindly increasing L_t is therefore not advisable. Our simulations suggest that maintaining the modulation length within the range of 5–7 mm offers an optimal trade-off between modulation efficiency and bandwidth, enabling a 3-dB bandwidth exceeding 260 GHz while keeping the V_π below 5 V. This satisfies the demands of emerging applications in ultra-high-speed, short-reach optical interconnects and terahertz signal processing. These findings offer valuable guidance for the future development of high-performance, broadband EO modulators.

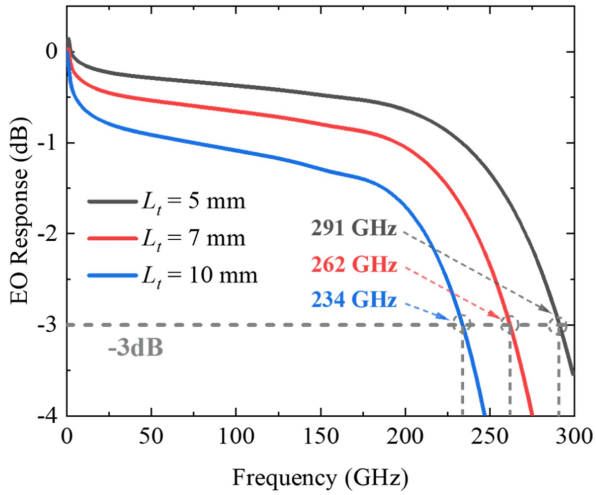

Fig. 12. Calculated EO response of the 5mm, 7 mm, and 10 mm long TFLN modulator with the optimized STWEs.

V. Conclusion

We have demonstrated an electrode optimization method for periodic structures based on the RGLC transmission line model, using STWEs as a representative example. Based on the fundamental electrical characteristics of the electrodes, we have derived, for the first time, analytical expressions that relate the equivalent circuit parameters of STWEs to their geometric design. This establishes a direct link between structural parameters and electromagnetic response. We further validated the method using TFLN modulators that show an ultra-high EO bandwidth of approximately 290 GHz, while maintaining a low voltage-length product of 2.5 V·cm, enabling both low power consumption and ultra-high-speed modulation.

In addition, the optimized STWEs feature large dimensions with a minimum linewidth of only 5 μm and a metal thickness as thin as 500 nm, making them highly compatible with low-cost and mature fabrication techniques such as deep UV lithography. This fabrication-friendly design significantly reduces process complexity and manufacturing cost, while enabling large-scale integration. The integration of STWEs with the TFLN platform further leverages the intrinsic advantages of TFLN, including low propagation loss, high modulation speed, and excellent thermal stability, thus offering critical support for scalable EO modulator arrays [33]. Moreover, by integrating TFLN modulators with on-chip silicon-based lasers and photodetectors, it becomes feasible to construct a complete monolithic photonic processing chain, paving the way toward future on-chip optical computing systems and reconfigurable optical interconnect platforms. The next step will be to verify the simulation results through experimental preparation. Moreover, the influence of electrode structure on temperature stability would be further investigated in order to improve the practical application of the proposed device.

ACKNOWLEDGMENT

The authors would like to thank Zhe Li, Daizhi Chen and Wenqi Yu for their valuable discussions and helpful comments.

REFERENCES

[1] Y. Ogiso et al., "80-GHz bandwidth and 1.5-V V_π InP-based IQ modulator," *J. Light. Technol.*, vol. 38, no. 2, pp. 249–255, Jan. 2020, doi: 10.1109/JLT.2019.2924671.

[2] J. Ozaki et al., "Over-85-GHz-bandwidth InP-based coherent driver modulator capable of 1-Tb/s/λ-class operation," *J. Light. Technol.*, vol. 41, no. 11, pp. 3290–3296, Jun. 2023, doi: 10.1109/JLT.2023.3236962.

[3] G. T. Reed, G. Mashanovich, F. Y. Gardes, and D. J. Thomson, "Silicon optical modulators," *Nat. Photon.*, vol. 4, no. 8, pp. 518–526, Aug. 2010, doi: 10.1038/nphoton.2010.179.

[4] A. Mohammadi, Z. Zheng, X. Zhang, L. A. Rusch, and W. Shi, "Segmented silicon modulator with a bandwidth beyond 67 GHz for high-speed signaling," *J. Light. Technol.*, vol. 41, no. 15, pp. 5059–5066, Aug. 2023, doi: 10.1109/JLT.2023.3250112.

[5] D. Zhu et al., "Integrated photonics on thin-film lithium niobate," *Adv. Opt. Photon.*, vol. 13, no. 2, Jun. 2021, Art. no. 242, doi: 10.1364/AOP.411024.

[6] M. Zhang, C. Wang, P. Kharel, D. Zhu, and M. Lončar, "Integrated lithium niobate electro-optic modulators: When performance meets scalability," *Optica*, vol. 8, no. 5, May 2021, Art. no. 652, doi: 10.1364/OPTICA.415762.

[7] G. Chen, Y. Gao, H.-L. Lin, and A. J. Danner, "Compact and efficient thin-film lithium niobate modulators," *Adv. Photon. Res.*, vol. 4, no. 12, Dec. 2023, Art. no. 2300229, doi: 10.1002/adpr.202300229.

[8] Y. Hu et al., "Integrated electro-optics on thin-film lithium niobate," *Nat. Rev. Phys.*, vol. 7, no. 5, pp. 237–254, Apr. 2025, doi: 10.1038/s42254-025-00825-5.

[9] C. Wang et al., "Integrated lithium niobate electro-optic modulators operating at CMOS-compatible voltages," *Nature*, vol. 562, no. 7725, pp. 101–104, Oct. 2018, doi: 10.1038/s41586-018-0551-y.

[10] P. Kharel, C. Reimer, K. Luke, L. He, and M. Zhang, "Breaking voltage–bandwidth limits in integrated lithium niobate modulators using micro-structured electrodes," *Optica*, vol. 8, no. 3, Mar. 2021, Art. no. 357, doi: 10.1364/OPTICA.416155.

[11] J. Tao, Y. Yang, X. Li, P. Wang, J. Li, and J. Liu, "Broadband thin-film lithium niobate electro-optic modulator," *Photonics*, vol. 11, no. 4, Mar. 2024, Art. no. 325, doi: 10.3390/photonics11040325.

[12] Z. Li et al., "Lithium niobate electro-optical modulator based on ion-cut wafer scale heterogeneous bonding on patterned SOI wafers," *Photon. Res*, vol. 13, no. 1, Jan. 2025, Art. no. 106, doi: 10.1364/PRJ.534954.

[13] X. Liu et al., "Wideband thin-film lithium niobate modulator with low half-wave-voltage length product," *Chin. Opt. Lett.*, vol. 19, no. 6, 2021, Art. no. 060016, doi: 10.3788/COL202119.060016.

[14] Z. Yu et al., "120 GHz sub-2 V thin-film lithium niobate modulators on silicon substrate using thick capacitively loaded slow wave electrodes," *IEEE Photon. J*, vol. 16, no. 6, Dec. 2024, Art. no. 7202305, doi: 10.1109/JPHOT.2024.3477311.

[15] X. Liu et al., "Capacitively-loaded thin-film lithium niobate modulator with ultra-flat frequency response," *IEEE Photon. Technol. Lett.*, vol. 34, no. 16, pp. 854–857, Aug. 2022, doi: 10.1109/LPT.2022.3178214.

[16] M. Jin, J. Chen, Y. Sua, P. Kumar, and Y. Huang, "Efficient electro-optical modulation on thin-film lithium niobate," *Opt. Lett.*, vol. 46, no. 8, pp. 1884–1887, Apr. 2021, doi: 10.1364/OL.419597.

[17] H. Liu et al., "Ultra-high-efficiency dual-band thin-film lithium niobate modulator incorporating low-K underfill with 220 GHz extrapolated bandwidth for 390 Gbit/s PAM8 transmission,".

[18] X. Liu et al., "Broadband capacitive-loaded thin-film lithium niobate modulator with on-chip terminal resistor," in *Proc. Asia Commun. Photon. Conf. 2021*, Shanghai, 2021, Art. no. T1I.5, doi: 10.1364/ACPC.2021.T1I.5.

[19] X. Liu et al., "Sub-terahertz bandwidth capactively-loaded thin-film lithium niobate electro-optic modulators based on an undercut structure," *Opt. Exp.*, vol. 29, no. 25, Dec. 2021, Art. no. 41798, doi: 10.1364/OE.442091.

[20] Y. Tang et al., "High performance thin-film lithium niobate modulator on silicon substrate with a thick silica buffer layer," *Opt. Exp.*, vol. 33, no. 10, May 2025, Art. no. 20334, doi: 10.1364/OE.560548.

[21] Z. Wang et al., "Silicon–lithium niobate hybrid intensity and coherent modulators using a periodic capacitively loaded traveling-wave electrode," *ACS Photon.*, vol. 9, no. 8, pp. 2668–2675, Aug. 2022, doi: 10.1021/acsphotonics.2c00263.

[22] G. Chen et al., "High performance thin-film lithium niobate modulator on a silicon substrate using periodic capacitively loaded traveling-wave electrode," *APL Photon.*, vol. 7, no. 2, Feb. 2022, Art. no. 026103, doi: 10.1063/5.0077232.

[23] F. Valdez et al., "110 GHz, 110 mW hybrid silicon-lithium niobate Mach-Zehnder modulator," *Sci. Rep.*, vol. 12, no. 1, Nov. 2022, Art. no. 18611, doi: 10.1038/s41598-022-23403-6.

[24] J. M. Fuster, J. Martí, and P. Candelas, "Modeling Mach–Zehnder $LiNbO_3$ external modulators in microwave optical systems," *Microw. Opt. Technol. Lett.*, vol. 30, no. 2, pp. 85–90, Jul. 2001, doi: 10.1002/mop.1228.

[25] Y. Liu, H. Li, J. Liu, S. Tan, Q. Lu, and W. Guo, "Low Vπ thin-film lithium niobate modulator fabricated with photolithography," *Opt. Exp.*, vol. 29, no. 5, Mar. 2021, Art. no. 6320, doi: 10.1364/OE.414250.

[26] Y. Li et al., "High-performance Mach–Zehnder modulator based on thin-film lithium niobate with low voltage-length product," *ACS Omega*, vol. 8, no. 10, pp. 9644–9651, Mar. 2023, doi: 10.1021/acsomega.3c00310.

[27] S. Sun et al., "High-speed modulator with integrated termination resistor based on hybrid silicon and lithium niobate platform," *J. Light. Technol.*, vol. 39, no. 4, pp. 1108–1115, Feb. 2021, doi: 10.1109/JLT.2020.3032786.

[28] A. Yariv and P. Yeh, *Photonics: Optical Electronics in Modern Communications, 6. Edition. in The Oxford Series in Electrical and Computer Engineering*. New York, NY, USA: Oxford Univ. Press, 2007.

[29] S. Haxha, B. M. A. Rahman, and K. T. V. Grattan, "Bandwidth estimation for ultra-high-speed lithium niobate modulators," *Appl. Opt.*, vol. 42, no. 15, May 2003, Art. no. 2674, doi: 10.1364/AO.42.002674.

[30] X. Xue et al., "High-performance thin-film lithium niobate Mach-Zehnder modulator on thick silica buffering layer," 2024, *arxiv:2412.12556*.

[31] M. Lin, Z. Li, J. Riemensberger, and T. J. Kippenberg, "Copper damascene process-based high-performance thin film lithium tantalate modulators," in CLEO 2025, Technical Digest Series, paper PD103_6, 2025.

[32] S. Shekhar et al., "Roadmapping the next generation of silicon photonics," *Nature Commun.*, vol. 15, no. 1, Jan. 2024, doi: 10.1038/s41467-024-44750-0.

[33] Y. Hu et al., "Integrated lithium niobate photonic computing circuit based on efficient and high-speed electro-optic conversion," *Nat. Commun.*, vol. 16, no. 1, Sep. 2025, Art. no. 8178, doi: 10.1038/s41467-025-62635-8.